SCIENCE CHINA
Information Sciences

• RESEARCH PAPER •

February 2026, Vol. 69, Iss. 2, 122404:1–122404:12
https://doi.org/10.1007/s11432-025-4610-5

Biomimetic cell in-situ self-healing PCL/CNT conductive composites for flexible pressure sensors with high sensitivity and wide linear measurement range

Xiangyu MENG[1], Hongyao TANG[2], Xiaozhou LÜ[3*], Jiayao ZHANG[1], Yaoguang SHI[3], Yumeng HE[4] & Weimin BAO[3]

[1]*School of Electronic Engineering, Xi'an University of Posts & Telecommunications, Xi'an 710121, China*
[2]*Science and Technology on Space Physics Laboratory, Beijing 100076, China*
[3]*School of Aerospace Science and Technology, Xidian University, Xi'an 710071, China*
[4]*Xi'an Aerospace Information Institute, Xi'an 710025, China*

Received 11 April 2025/Revised 23 June 2025/Accepted 18 September 2025/Published online 4 January 2026

Abstract Flexible pressure sensors are widely used in wearable electronic devices, human motion detection, and electronic skin. Conductive composites are the core component of flexible pressure sensors. However, they suffer from mechanical damage during long-term cycling, which degrades sensor performance. This study proposed a biomimetic cell in-situ self-healing polycaprolactone/carbon nanotube composite (BCISPC). The core-shell structure of BCISPC endows the composite with a low percolation threshold (0.012 vol%), high electrical conductivity (13.3 S/m), and fast electrothermal self-healing capability (18 s). The efficient in-situ self-healing ability of the composite preserves its surface microstructure during self-healing. In addition, a self-healing hierarchical microstructured flexible pressure sensor was prepared using BCISPC. The sensor has a high sensitivity (159.4 kPa^{-1}), wide linear measurement range (0–500 kPa), fast response time (34 ms), and good cycling durability (1000 cycles). Given its high performance, this sensor has various applications in wearable electronics, medical monitoring, and human-machine interfaces.

Keywords biomimetic cell, self-healing, flexible pressure sensor, hierarchical microstructure, high sensitivity, wide linear measurement range

Citation Meng X Y, Tang H Y, Lü X Z, et al. Biomimetic cell in-situ self-healing PCL/CNT conductive composites for flexible pressure sensors with high sensitivity and wide linear measurement range. Sci China Inf Sci, 2026, 69(2): 122404, https://doi.org/10.1007/s11432-025-4610-5

1 Introduction

Flexible pressure sensors have received increasing attention owing to their ability to convert stimuli of interest into electrical signals for use in applications such as human motion detection [1–3], electronic skin [4–6], health monitoring [7–9], and human-computer interaction [10–12]. Conductive composites are the key components of flexible pressure sensors, which comprise a substrate material and a conductive filler. Elastomers such as polydimethylsiloxane (PDMS) [13–15] and Ecoflex [16–18], which have good elasticity, flexibility, and stretchability, are considered good candidates among the available options for substrate materials. However, these conventional elastomeric materials are permanently cross-linked networks that cannot be recovered once damaged. The damage to the conductive composite material caused by frequent long-term cycling of external forces can adversely affect sensor performance.

Researchers developed self-healing conductive composites to address the issues above [19–22]. These conductive composites can be broadly classified into extrinsic and intrinsic. Extrinsic self-healing is achieved by embedding healing agents in conductive composites. When extrinsic self-healing conductive composites are damaged, the embedded healing agent is released, and external self-healing occurs [23]. This healing mechanism immediately restores conductivity. However, it requires consuming pre-embedded healing agents, resulting in limited healing times and unrepeatable healing at the exact location. By contrast, intrinsic self-healing conductive composites do not require adding healing agents, and the damaged regions can be repeatedly healed through polymer matrix recombination [24,25]. The polymer matrix is reconstructed via the regeneration of dynamic covalent or noncovalent bonds and the entanglement of polymer chains at the damaged interface. Intrinsic self-healing conductive composites

* Corresponding author (email: xzlu@xidian.edu.cn)

© Science China Press 2026

have shown greater potential applications and attracted more research than extrinsic ones. Li et al. [26] reported a self-healing conductive composite based on the synergistic hydrogen bond interaction between poly (polymerizable deep eutectic solvents) and phytic acid molecules. This conductive composite has a conductivity of 7.8×10^{-4} S/cm. After 48 h of self-healing, the conductivity of the composite can be restored to 91.5% of the initial value. Min et al. [27] prepared a room-temperature self-healing conductive composite based on imine reversible covalent bonds by introducing carbon nanotubes (CNTs) and carbon black. The composite has a resistivity of 108 Ω·m and an electrical self-healing rate of up to 93% under 100°C hot pressing. Yu et al. [28] prepared self-healing polydimethylsiloxane (PDMS) by introducing intermolecular dynamic hydrogen bonds and reversible dynamic imine bonds into the molecular network structure of PDMS. CNTs were incorporated into self-healing PDMS to prepare self-healing conductive composites. These composites can achieve self-healing at 60°C for 18 h, and their electrical self-healing efficiency is as high as 97.8%. Kong et al. [29] reported a conductive composite material based on epoxy natural rubber, lipoic acid, and CNTs. The composite has a conductivity of 0.77 S/m and a self-healing ability. Moreover, it can achieve 100% self-healing efficiency under an applied voltage of 20 V for 4 h.

The studies above have made substantial advances in self-healing composites. However, some challenges need to be addressed. The self-healing of conductive composites is time-consuming, which makes this process cost-ineffective. Furthermore, researchers usually introduce microstructures on the surface of the sensitive material in sensors to improve their sensing performance; however, preserving the morphology of the microstructures during self-healing is difficult, adversely affecting sensor performance after self-healing.

The electrical stimulation of the human skin after wounding can accelerate cell migration and proliferation to promote wound self-healing. Thus, this study proposed a biomimetic cell in-situ self-healing polycaprolactone (PCL)/CNT composite (BCISPC). Hot pressing endowed the composite with an efficient segregated conductive network, resulting in a low percolation threshold and high conductivity. The percolation threshold could be further reduced by adjusting the size of the PCL particles. The low melting point and high electrical conductivity allowed BCISPC to have localized rapid electrothermal self-healing capability and the ability to ensure intact surface microstructure during self-healing. Moreover, a self-healing flexible pressure sensor was prepared using hierarchical microstructured BCISPC, and the sensitivity and linear measurement range of the sensor were improved by adjusting the shape and hierarchical microstructure of this composite. Furthermore, the sensor exhibited excellent sensing characteristics such as self-healing ability, high sensitivity, and a wide linear measurement range, indicating its broad application potential in human motion detection and other fields.

2 Material and methods

2.1 Design ideas and self-healing principles of BCISPC

When human skin is wounded, directional cell migration and proliferation can be promoted via external electrical stimulation, thereby accelerating wound healing (Figure 1(a)) [30]. Thus, we designed a biomimetic cell structure, i.e., BCISPC, which comprised an internal thermoplastic polymer mimicking the cytoplasm and an external conductive network mimicking the cell membrane. When BCISPC was stimulated by an external voltage, its high electrical conductivity allowed its broken part to heat up rapidly, and the internal thermoplastic polymer transformed from a crystal state to a melted state, increasing composite fluidity and facilitating composite healing (Figure 1(b)). For fabricating BCISPC, PCL, which has a low melting point (54.5°C), was used as the thermoplastic polymer, and CNTs, which have good electrical conductivity, were used as the conductive network.

Figure 1(c) shows the in-situ self-healing principle of BCISPC. The PCL and CNTs inside the composite formed a biomimetic cell core-shell structure. The PCL constituted the inner core, providing the composite self-healing ability. The CNTs constituted the outer shell, which endowed the composite with conductivity. When BCISPC was broken, the core-shell structure was damaged, and the conductive network of CNTs inside was broken. After aligning the broken part, the conductive network was reproducibly linked, but the internal PCL remained in the broken state. Applying a voltage to both sides of BCISPC increased the temperature at the broken part drastically because of its good conductivity. The internal PCL changed from crystal to melted, and the PCL surfaces at the broken part rebonded together. When the temperature decreased to room temperature, the PCL at the broken part recrystallized to form a new core-shell structure, and BCISPC underwent complete in situ self-healing.

2.2 Materials

PCL (PCL 6500, Mn = 50000) was obtained from Perstorp Limited, UK. CNTs (XFM13, diameter: 10–20 nm, length: 10–30 μm, and purity: > 98%) were ordered from Jiangsu XFNANO Materials Tech Co., Ltd. Ecoflex (00-

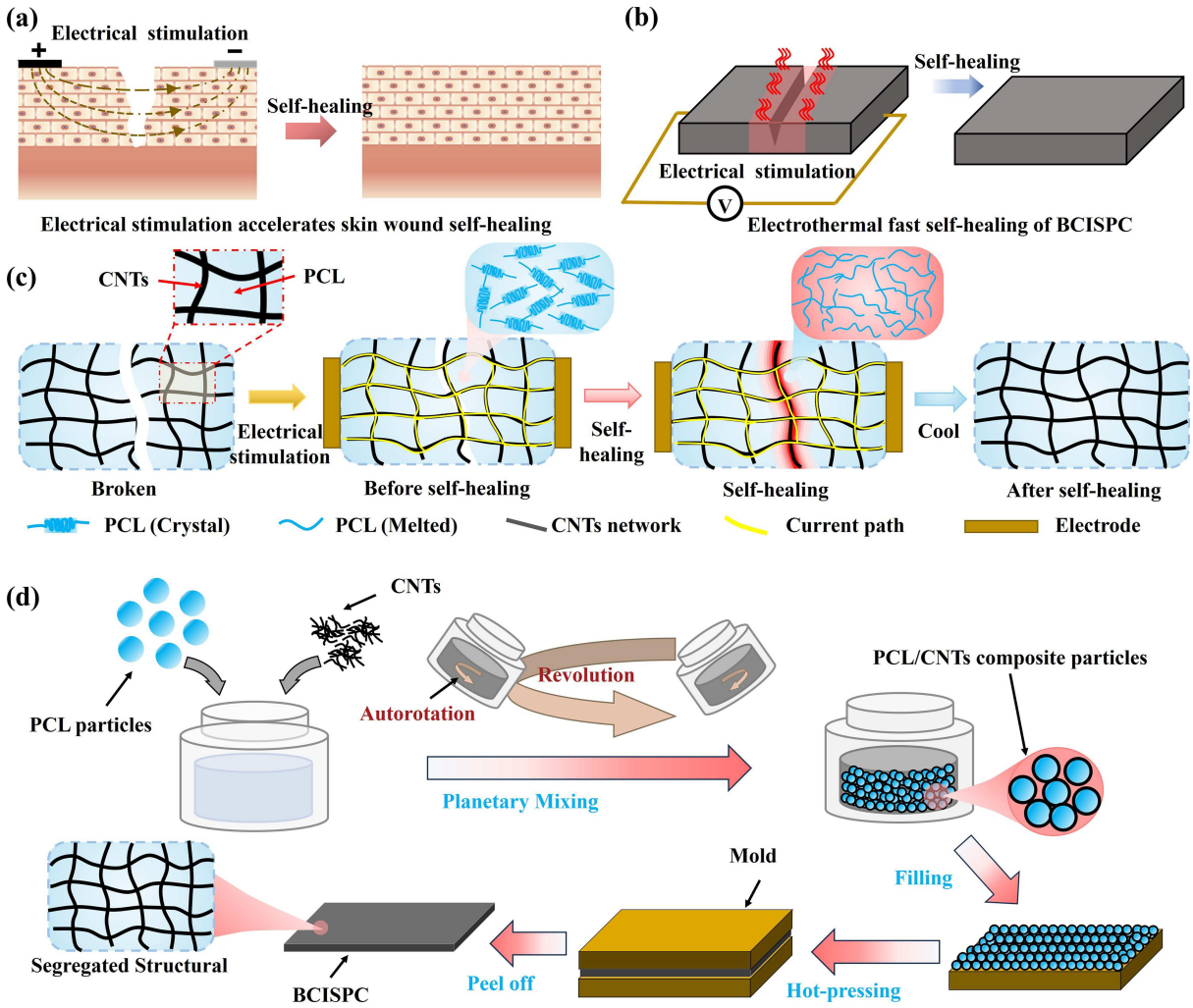

Figure 1 (Color online) Schematic representation of the electrically stimulated in-situ self-healing of (a) skin wounds and (b) BCISPC; (c) principal diagram of the in-situ self-healing of BCISPC; (d) schematic representation of the preparation process of BCISPC.

30) was purchased from Smooth-On, Inc., PA, USA. Ag flakes (diameter: 10 μm) were purchased from Xingrongyuan Metal Materials Company Ltd., Hebei, China. Shanghai Aladdin Biochemical Technology ordered petroleum ether (AR, bp 30°C–60°C).

2.3 Preparation of BCISPC

The preparation process of BCISPC is shown in Figure 1(d). PCL particles were separated into samples of different particle sizes using 60, 80, 100, 140, and 300 mesh sieves. The PCL particles with a size between 60 and 80 mesh, 80 and 100 mesh, 100 and 140 mesh, and 140 and 300 mesh were denoted as PCL-60-80, PCL-80-100, PCL-100-140, and PCL-140-300, respectively. The scanning electron microscopy (SEM) and optical photographs of the PCL particles with different sizes are shown in Figures 2(a) and S1. The PCL particles and CNTs were placed in a vial, and the mixed powders were mixed at room temperature for 5 min using a planetary mixer (HMV800, Shenzhen Hassai Technology Co., Ltd., Shenzhen, China) to obtain the core-shell structure of the PCL/CNT composite particles. These particles were wrapped with a layer of CNTs (Figures 2(b) and S2), filled into a hot-pressing mold, and heated to 70°C under 10 kPa pressure for 10 min. BCISPC was peeled off from the mold after the mold cooled to room temperature.

2.4 Preparation of the flexible pressure sensor

A hot-pressing mold with a hierarchical microstructure was prepared using 3D printing. Hierarchical microstructured BCISPC was prepared using this mold according to the method discussed in Subsection 2.3. Ag/Ecoflex electrodes

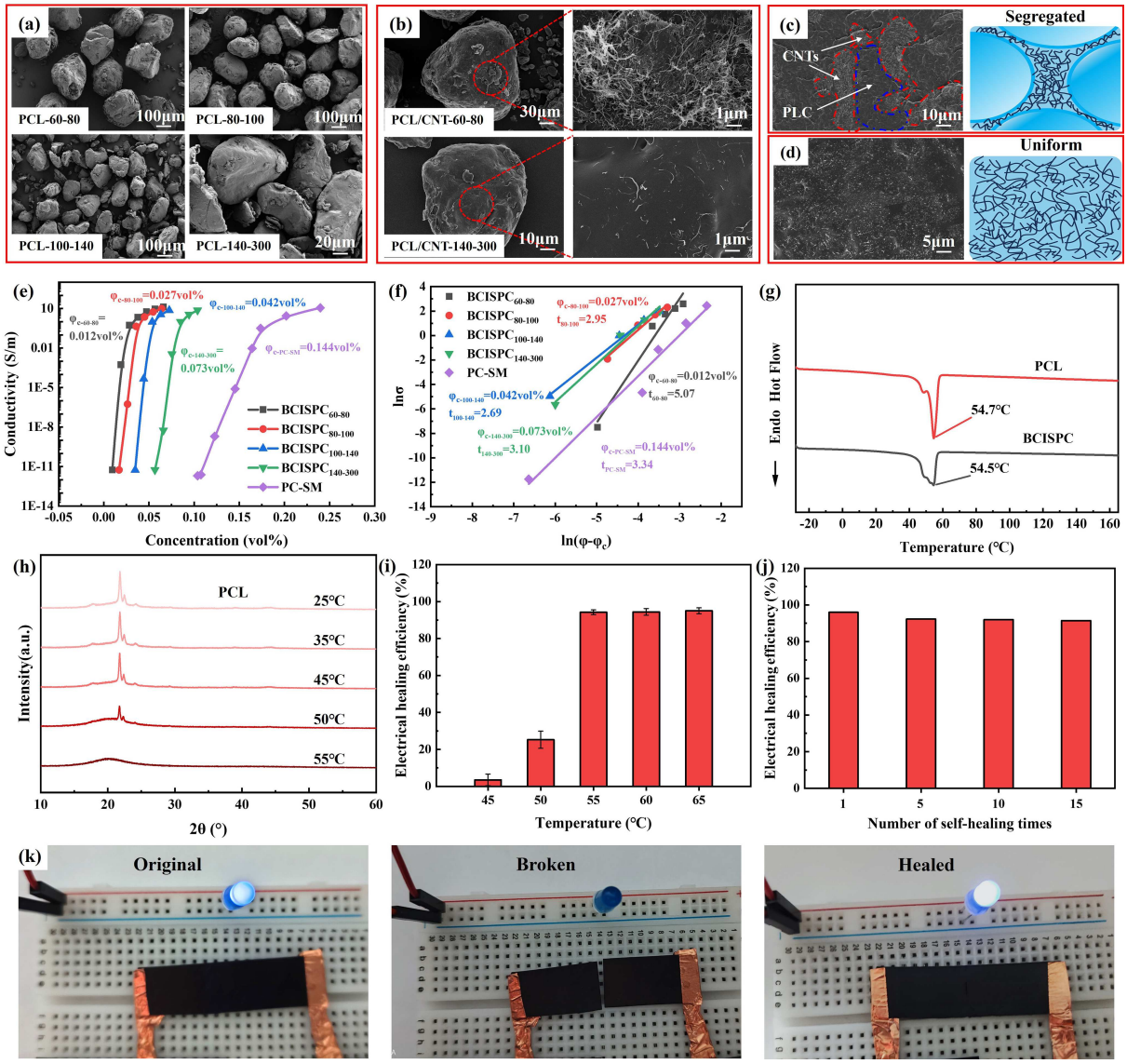

Figure 2 (Color online) SEM images of (a) PCL particles and (b) PCL/CNT composite particles of different sizes. Cross-sectional SEM images and schematic illustration of the microstructure of (c) BCISPC and (d) PC-SM. (e) The conductivity of BCISPC and PC-SM at different CNT concentrations. (f) The log-log plot of conductivity with $\varphi - \varphi_c$ for $\varphi > \varphi_c$. (g) DSC curves of the second heating segment of PCL and BCISPC. (h) XRD curves of PCL at different temperatures. Relationship between electrical healing efficiency and (i) heating temperature and (j) healing times. (k) The BCISPC is connected to the circuit as a conductor.

were prepared using screen printing. The specific process is described as follows. First, Ag inks (Ag content 75 wt%) were prepared using a planetary mixer with petroleum ether as the solvent and Ecoflex as the crosslinking agent. Second, Ecoflex substrate films were prepared using casting. Finally, Ag ink was printed onto the Ecoflex films using screen printing. The Ecoflex films printed with Ag ink were left at 170°C for four hours to remove petroleum ether, and the ink was cured to obtain Ag/Ecoflex electrodes. Finally, the flexible pressure sensor was obtained by assembling the prepared components. The structure of the sensor is shown in Figure S3.

2.5 Characterization

The micromorphology of the samples was characterized using a scanning electron microscope (ZEISS Sigma 300, Germany). The samples were plated with a thin layer of gold before testing. The samples' thermal properties were investigated using a differential scanning calorimeter (Mettler DSC3) under a nitrogen atmosphere. The samples were heated to 170°C at a heating rate of 10°C/min and maintained for 5 min to eliminate any prior thermal history. Subsequently, the samples were cooled to −30°C at 10°C/min to obtain the cooling curves. Finally, the samples were heated to 170°C at the same scanning rate to obtain the heating curves. X-ray diffraction (XRD)

analysis was conducted using an X-ray diffractometer (Rigaku SmartLab SE) within a 2θ angle range of 10° to 60° with Cu Kα radiation ($\lambda = 0.154056$ nm) at a scanning speed of 10°/min to characterize the crystalline phase of the samples. The electrical resistance of the BCISPC was measured using a digital multimeter (DMM 6500, Keithley). The electrical conductivity of BCISPC was calculated as $\sigma = l/(RC)$, where l is the length, R is the resistance, and C is the cross-sectional area. A Keithley 2450 source meter was used to provide a DC voltage of 10 V during the electrothermal self-healing of BCISPC. The self-healing process was thermally imaged using an infrared thermal camera (VICTOR-360, Shenzhen Yisheng Victory Technology Co., Ltd., Shenzhen, China). Furthermore, the Keithley 2450 source meter was used to record the real-time current value of the pressure sensor at 1 V.

3 Results and discussion

3.1 Segregated structural conductive networks for BCISPC

$BCISPC_{a\text{-}b}$ was prepared by hot pressing using PCL particles with different sizes. a-b represents BCISPC prepared using PCL-a-b particles (a-b is specifically defined in Subsection 2.3 Preparation of BCISPC). The classification methods and numbering of PCL particles of different sizes were described in Subsection 2.3. For comparison, PCL/CNT composites were prepared using the solvent method (PC-SM). Figures 2(c) and (d) show the cross-sectional SEM images of BCISPC and PC-SM, respectively. PC-SM has uniform conductive networks, while BCISPC has conductive networks with segregated structures, such as cells (CNTs are concentrated in a certain area). The conductivity of all samples was measured (Figure 2(e)). The trend of sample conductivity with CNT content was consistent with the percolation theory. The CNT particles did not form a complete conductive network at low concentrations, and the composite exhibited an insulating state. However, when the amount of filler particles in the matrix reached a certain value, which is known as the percolation threshold, the conductivity of the composite increased drastically. The conductivity of the composite was fitted using the following equation [31]:

$$\sigma = \sigma_c(\varphi - \varphi_c)^t, \tag{1}$$

where σ is the conductivity of the composite, σ_c is the conductivity of CNTs, φ is the volume fraction of CNTs, φ_C is the percolation threshold, and t is the critical index. The fitting results are shown in Figure 2(f). BCISPC showed a low percolation threshold. The percolation thresholds of $BCISPC_{60\text{-}80}$ and PC-SM were 0.012 and 0.144 vol%, respectively. These results indicate that the BCISPC can form an effective conductive pathway at a low CNT content. This phenomenon is attributed to the segregated structural conductive network, which can concentrate the CNTs in the interfacial region of the PCL particles and increase the effective content of the CNTs in this region. In addition, the larger the PCL particles, the lower the percolation threshold of BCISPC. When the PCL particles were 200–300 μm (PCL-60-80), 150–200 μm (PCL-80-100), 106–150 μm (PCL-100-140), and 50–106 μm (PCL-140-300) in size, the percolation thresholds of BCISPC were 0.012, 0.027, 0.042, and 0.073 vol%, respectively. Therefore, the larger the PCL particles, the smaller the proportion of the interfacial region enriched with CNTs. Moreover, the smaller the interfacial region, the less conductive filler is required to achieve the same effective content. As shown in Figures 2(b) and S2, the smaller the particle, the fewer the CNTs encapsulated on its surface. When the weight of PCL is the same, a smaller particle size means more particles. An increase in particle size indicates a larger area available for CNT attachment, resulting in a lower CNT attachment density. Furthermore, the larger the PCL particles, the lower the percolation threshold of BCISPC.

Furthermore, the effect of CNT concentration on the Young's modulus of BCISPC was investigated; the results are shown in Figure S4. BCISPC with a CNT concentration of 0.066 vol% had the lowest Young's modulus, indicating the best mechanical flexibility. Moreover, it exhibited the highest conductivity (13.3 S/m). Therefore, BCISPC with this concentration was selected for subsequent experiments.

3.2 Self-healing behavior of BCISPC

PCL is a linear polymer material with good thermoplasticity, which provides favorable conditions for the self-healing of BCISPC. According to the self-healing principle shown in Figure 1(c), the melting point of PCL is a key factor in the self-healing of BCISPC. In this study, the thermal properties of PCL and BCISPC were investigated. The DSC data for the cooling and secondary heating of PCL and BCISPC composites are shown in Figures S5 and 2(g). The melting point (T_m) in BCISPC (54.5°C) is close to that of pure PCL (54.7°C), indicating that the addition of CNTs did not remarkably disrupt the crystalline structure of PCL. BCISPC can be melted at a low processing temperature, improving self-healing properties. In addition, in-situ variable-temperature XRD tests were conducted on PCL and BCISPC; the results are shown in Figures 2(h) and S6. When the temperature is below 45°C, two

diffraction peaks are observed at Bragg angles of 21.7° and 23.9°, respectively; these diffraction peaks correspond to the (110) and (200) lattice faces of the PCL semicrystalline structure, respectively. When the temperature is raised to 50°C, the intensity of the two diffraction peaks remarkably decreases, indicating a reduction in the crystallinity of PCL. When the temperature is raised to 55°C, the diffraction peaks disappear and PCL transitions to a molten state. The results for BCISPC are similar to those for PCL, indicating that CNTs do not influence the temperature-dependent crystallinity changes in PCL. Therefore, the increase in temperature to 55°C is conducive to the self-healing ability of BCISPC.

Furthermore, the self-healing ability of BCISPC was investigated. A broken BCISPC was placed on a heating platform for 1 min, and its conductivity was measured after it had been cooled down. The electrical healing efficiency (EHE) of BCISPC was calculated as follows:

$$\mathrm{EHE} = (\sigma_{\mathrm{se}} - \sigma_0) \times 100\%, \tag{2}$$

where σ_0 is the conductivity of the BCISPC in the original state, and σ_{se} is the conductivity of the BCISPC after self-healing. First, the effect of temperature on EHE was investigated; the results are shown in Figure 2(i). When the temperature is <55°C, EHE is <30%. When the temperature increases to 55°C, EHE increases to 94.2%. When the temperature continues to increase, EHE remains basically unchanged. When the temperature is lower than the melting point of BCISPC (54.4°C), the PCL molecules cannot transform from the crystal state to the melted state; therefore, EHE decreases. When the temperature increases above the melting point of BCISPC, the PCL molecules absorb more heat to transform from the crystal state to the melted state and complete the self-healing process. This finding is consistent with the result presented in Figure 2(h). Second, the effect of healing times on EHE was investigated. Figures S7 and 2(j) show the relationship between healing times and EHE resistance. We found that the resistance of the BCISPC increased slightly after the first self-healing compared with the original state. When the healing times are greater than 5, EHE remains basically unchanged (∼92%). Finally, as a demonstration, we connected BCISPC as a conductor into the circuit (Figure 2(k)). The healed BCISPC still exhibited good conductivity.

In addition, the mechanical properties were investigated after self-healing; the results are shown in Figures S8(a) and (b). The mechanical healing efficiency (MHE) of BCISPC was calculated as follows:

$$\mathrm{MHE} = (S_{\mathrm{healed}} - S_{\mathrm{original}}) \times 100\%, \tag{3}$$

where S_{healed} and S_{original} indicate the tensile strength of the self-healing and original specimens, respectively. MHE decreases with increasing self-healing times, and when the self-healing times reach ⩾10, MHE stabilizes at ∼82%.

Given its good electrical conductivity, BCISPC can undergo electrothermal in-situ self-healing, unlike many self-healing composites. The electrothermal self-healing process is shown in Figure 3(a). A voltage of 30 V was applied to both ends of the broken BCISPC, and it took only 18 s for this BCISPC to self-heal. The temperature of the BCISPC during electrothermal heating was recorded using an infrared camera (Figure 3(b)). Photographs of the BCISPC before and after self-healing are shown in Figure 3(c). The heating power (P) equation is presented as follows:

$$P = (U^2/R), \tag{4}$$

where P is large because the resistance of the BCISPC is small (∼60 Ω). The initial temperature of the BCISPC was 28.6°C (close to room temperature). The temperature on the surface of the BCISPC increased rapidly when the voltage was turned on, reaching 36.0°C at 2 s, 42.0°C at 10 s, and 59.1°C at 18 s. The high conductivity of BCISPC endows it with electrothermal in-situ self-healing ability. Furthermore, the effect of voltage on the heating process was investigated in this study. The results are shown in Figure 3(d). The self-healing time of BCISPC increases with decreasing voltage. The self-healing time of BCISPC was 18, 131, and 494 s when the voltage was 30, 25, and 20 V, respectively.

Furthermore, microstructured BCISPC was prepared, and its electrothermal in-situ self-healing ability was investigated; the results are shown in Figure 3(e). The microstructural morphology of the BCISPC surface remained unchanged after self-healing because the heating power was mainly concentrated at the broken part. This phenomenon provides a basis for preparing high-performance flexible pressure sensors with self-healing capability.

The healing rate (HR) is defined as follows:

$$\mathrm{HR} = \mathrm{EHE}/\mathrm{HT}, \tag{5}$$

where EHE is the electrical healing efficiency, and HT is the healing time. Finally, the EHE, HT, and HR of BCISPC were compared with most of its counterparts reported in literature; the results are shown in Figure 3(f) and Table S1 [32–48]. The BCISPC has a high HR of 314%/min, a high EHE of 94.2%, and a low HT of 0.3 min.

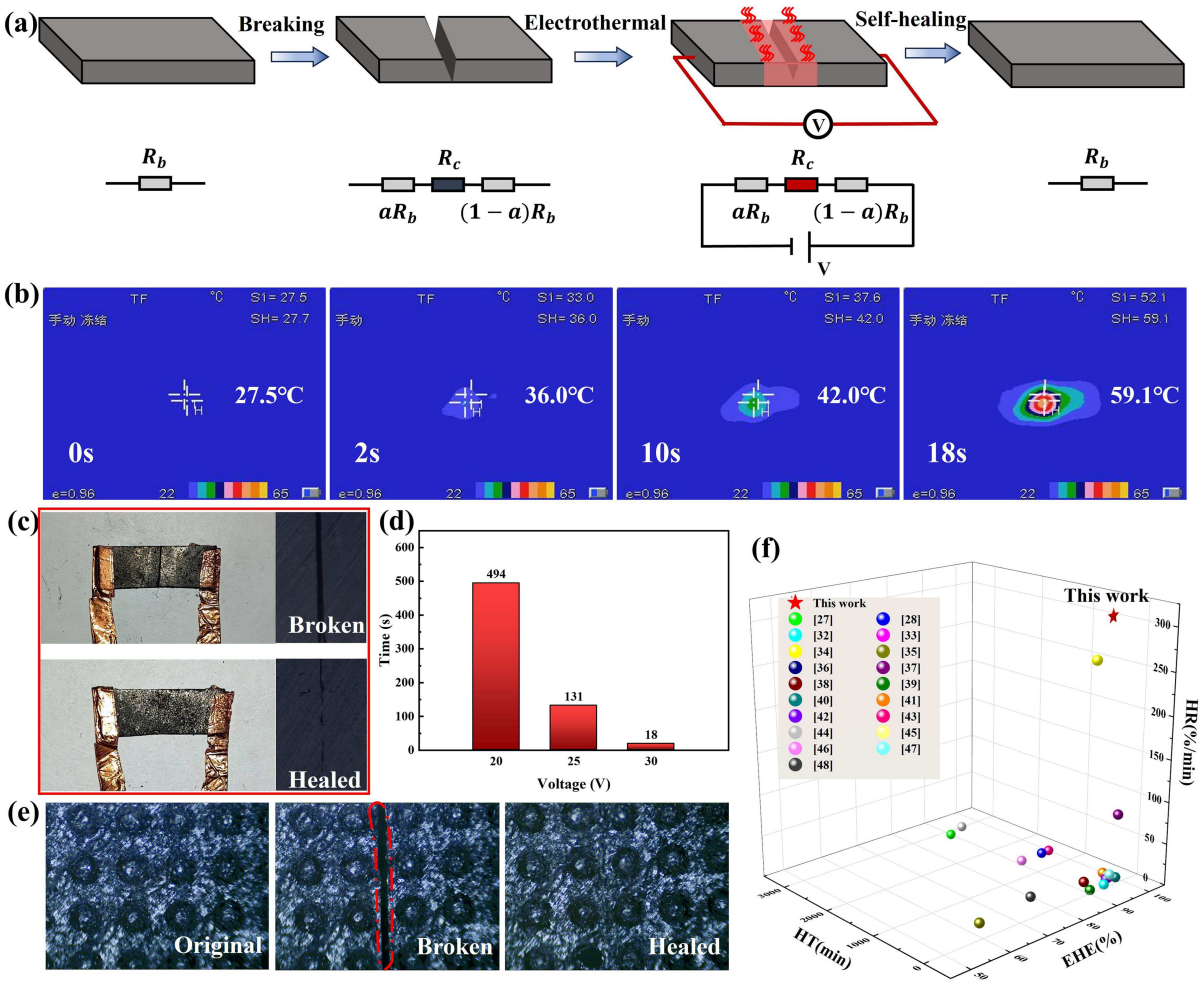

Figure 3 (Color online) (a) Schematic illustration of the electrothermal in-situ self-healing ability of BCISPC; (b) temperature of the BCISPC surface during electrothermal in-situ self-healing; (c) photographs of the broken BCISPC before and after self-healing; (d) relationship between the applied voltage and self-healing time; (e) photographs of the microstructured BCISPC before and after in-situ self-healing; (f) comparisons of the EHE, HT, and HR of BCISPC with those of the counterparts of BCISPC reported in the literature.

3.3 Design concept and performance of flexible pressure sensors

The application of microstructured BCISPC to flexible pressure sensors can maintain their performance (sensitivity and linear measurement range) without degradation after self-healing. The microstructure of BCISPC was designed to provide a flexible pressure sensor with high sensitivity and a wide linear measurement range. Figure 4(a) shows the sensor's sensing principle. When the sensor is under pressure, the microstructure is compressed and deformed; the contact area between the composite material and the electrode increases, and the contact resistance decreases. According to the electrical contact theory, the contact resistance (R_c) can be expressed as follows [49]:

$$R_c = \frac{1}{2k\sqrt{A}/\pi}, \tag{6}$$

where k is the equivalent conductivity of the two contacting objects and A is the contact area. The sensitivity of the pressure sensor can be expressed as follows:

$$S = \frac{\mathrm{d}(\Delta I/I_0)}{\mathrm{d}p}, \tag{7}$$

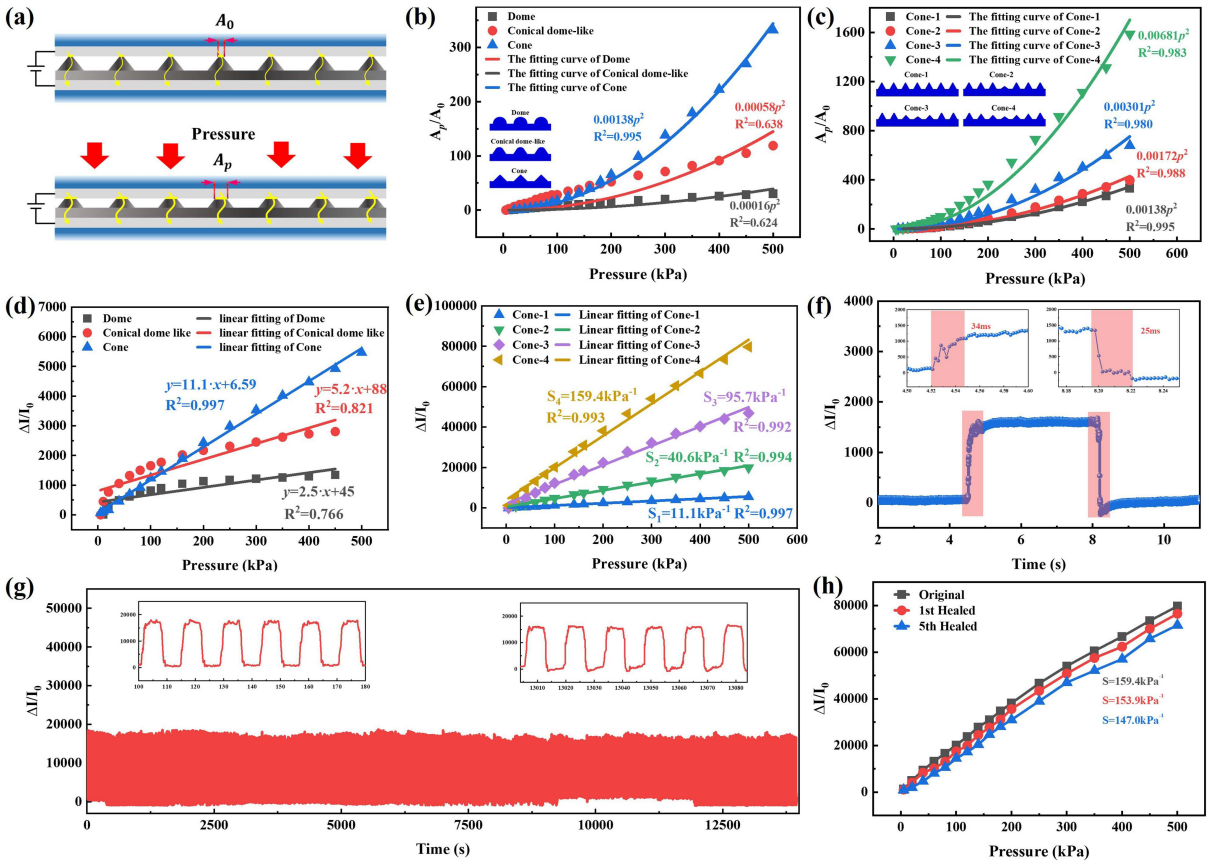

Figure 4 (Color online) (a) Working principle diagram of the flexible pressure sensor. Finite element simulation data of the contact area versus pressure for (b) three uniform microstructures (dome, conical dome-like, and cone) and (c) different hierarchical microstructures (cone-1, cone-2, cone-3, and cone-4). Piezoresistive characterization of pressure sensors for (d) dome, conical dome-like, and cone, as well as (e) cone-1, cone-2, cone-3, and cone-4. (f) Response time of the sensor. (g) Pressure sensing response during cyclic loading (1000 times at 100 kPa). (h) Piezoresistive characterization of the original and healed sensor.

where ΔI is the value of current change, I_0 is the initial current, and p is the pressure. According to Ohm's law, the relative change in current ($\Delta I/I_0$) caused by pressure can be written as follows:

$$\frac{\Delta I}{I_0} = \frac{R_{c0} - R_{cp}}{R_{cp}} = \frac{\frac{1}{2k\sqrt{A_0}/\pi} - \frac{1}{2k\sqrt{A_p}/\pi}}{\frac{1}{2k\sqrt{A_p}/\pi}} = \sqrt{A_p/A_0} - 1, \tag{8}$$

where A_p is the function of pressure p such that $\sqrt{A_p/A_0} = f(p)$. Thus, rewriting the sensitivity equation yields the following equation:

$$S = \frac{\mathrm{d}(\Delta I/I_0)}{\mathrm{d}p} = \frac{\mathrm{d}(\sqrt{A_p/A_0} - 1)}{\mathrm{d}p} = \frac{\mathrm{d}(\sqrt{A_p/A_0})}{\mathrm{d}p} = f'(p). \tag{9}$$

If the sensor has good linearity, then the sensitivity is a constant independent of the pressure p, i.e., $\sqrt{A_p/A_0}$ is a primary function of p, $\sqrt{A_p/A_0} = ap + b$, $A_p/A_0 = (ap + b)^2$, and A_p/A_0 is a quadratic function of p, wherein a, b are constants and $a \neq 0$. Therefore, sensors with high sensitivity and a wide linear range can be obtained using a structural design (making A_p/A_0 a quadratic function of p and increasing the value of a).

In this study, the deformation and contact area changes of three microstructures, namely, dome, conical dome-like, and cone, under pressure were investigated using finite element analysis to obtain microstructures with a good linear measurement range (Figures 4(b) and S9). The contact area of all three structures increases with increasing pressure. Quadratic functions were fitted to the data shown in Figure 4(b), and R^2 was calculated. The closer the R^2 value is to 1, the better the fit. The R^2 values for dome, conical dome-like, and cone were 0.624, 0.638, and 0.995, respectively. The results indicate that the contact area versus the pressure curve of the cone is closer to a quadratic function than that of the dome and conical dome-like. Cone exhibits better linearity.

Based on previous analysis, the sensor's sensitivity increases with increasing a. The use of hierarchical microstructures can effectively increase the sensitivity. Relative to uniform structures, hierarchical microstructures

can effectively reduce the initial contact area by reducing the number of microstructures in contact with the electrode in the initial state (Figure S10). Based on (8), reducing the initial contact area A_0 can improve the sensor's sensitivity. Furthermore, with increasing pressure, the hierarchical microstructure can contact the electrode hierarchically through different levels of microstructures. Consequently, the sensor with this structure can provide a relative variation in the contact area of the whole pressure range. Four hierarchical conical microstructures, namely, cone-1, cone-2, cone-3, and cone-4, were designed, where the numbers represent the number of hierarchies (cone-1 is a highly uniform microstructure). The four microstructures' deformation and contact area changes under pressure loading were analyzed using finite elements (Figures 4(c) and S11). With increasing pressure, the microstructure is gradually compressed from high to short, gradually increasing the contact area. The initially smaller contact area of hierarchical microstructures causes a greater variation at the same applied pressure than uniform microstructures. Using the least squares method, a quadratic function was fitted to the data presented in Figure 4(c). The quadratic term coefficient of the fitted curve increases with the number of hierarchies. When the hierarchy is 1, the quadratic term coefficient is 0.00138. When the hierarchy is 2, 3, and 4, the quadratic term coefficient increases to 0.00172, 0.00301, and 0.00681, accounting for 24%, 118%, and 393%, respectively, compared to 1. Meanwhile, the R^2 values of the fitted curves are all greater than 0.98, ensuring the sensor's linearity. Based on the aforementioned finite element simulation, the conductive sensitive layer with a cone microstructure has better linearity, while the sensor's sensitivity can be improved by introducing the hierarchical microstructure.

Different microstructured BCISPCs were prepared and utilized to prepare pressure sensors. Figure S12 shows the optical microscopic images of the microstructured BCISPC. Figure 4(d) shows the piezoresistive characteristics of the flexible pressure sensors with uniform microstructures. The R^2 values of the fitted straight lines of the piezoresistive characteristics of the sensor are 0.997, 0.821, and 0.766, respectively. This result indicates that the cone structure has good linearity, and the conical dome-like and dome structures exhibit remarkable nonlinearity, consistent with the results of theoretical and simulation analyses.

The slope of the fitted curve indicates the sensor's sensitivity. The sensitivity of the uniform cone structure sensor is only 11.1 kPa^{-1}. In this study, pressure sensors with hierarchical microstructures were designed to improve the sensor's sensitivity. Figure 4(e) shows the piezoresistive characteristics of the sensors. The sensitivity of the cone-2 sensor is 40.6 kPa^{-1}, which accounts for a 266% increase in sensitivity compared to cone-1. The sensitivity of the sensors increased gradually with increasing hierarchy. The sensitivities of cone-3 and cone-4 were 95.7 and 159.4 kPa^{-1}, 762% and 1,336% higher than those of cone-1, respectively. Meanwhile, the R^2 values of the sensors were 0.996, 0.994, 0.992, and 0.993, which indicated the good linearity of the sensors. Furthermore, the response time and cyclic endurance characteristics of the cone-4 sensor were tested. As shown in Figure 4(f), the sensor has a fast response time (rise and fall times of 34 and 25 ms, respectively). The sensor was repeatedly loaded 1000 times at 100 kPa; no considerable degradation in its response was observed (Figure 4(g)). An Ag/Ecolfex electrode contributed markedly to the sensor's robustness. This electrode comprised an Ag/Ecoflex conductive layer and an Ecoflex substrate layer (Figure S13). The Ag/Ecoflex electrode surface did not develop cracks after cycling, which could decrease sensor performance (Figures S14(a) and (b)). Based on the stretching test results, the Ag/Ecoflex electrode did not crack after repeated loading because of its good elasticity (Figures S15(a) and (b)). Furthermore, sensors were prepared using microstructured BCISPCs that self-healed one and five times, and their piezoresistive properties were characterized (Figure 4(h)). After self-healing one and five times, the sensitivities were 153.9 and 147.0 kPa^{-1}, respectively. In addition, the sensors prepared using BCISPCs healed five times with 1000 cycles of 100 kPa were tested; the results are shown in Figure S16. The sensor prepared using self-healed BCISPCs exhibits good sensitivity and cyclic stability.

Furthermore, the effects of temperature and humidity on sensor performance were investigated to confirm the environmental robustness of the sensor. In investigating the effect of temperature on the sensor, air conditioning was used to control the laboratory temperature. The sensor was placed in a constant-temperature environment for 30 min for testing. The piezoresistive characteristics of the sensor were measured at different temperatures; the results are shown in Figure S17. The piezoresistive characteristics are not affected by temperature. In studying the effect of humidity on the sensor, the sensor was placed in a drying oven or above a humidifier for 30 min before testing. The piezoresistive characteristics of the sensor under different humidity conditions are shown in Figure S18. Humidity does not affect sensor performance. This phenomenon may be attributed to the fact that Ecoflex has good airtightness, which ensures the sensor's environmental robustness. The performance of the as-prepared sensor was compared with that of the previously reported sensors (Table S2). Compared with the previously reported sensors, the as-prepared sensor exhibits excellent performance with regard to sensitivity, linear measurement range, and response time.

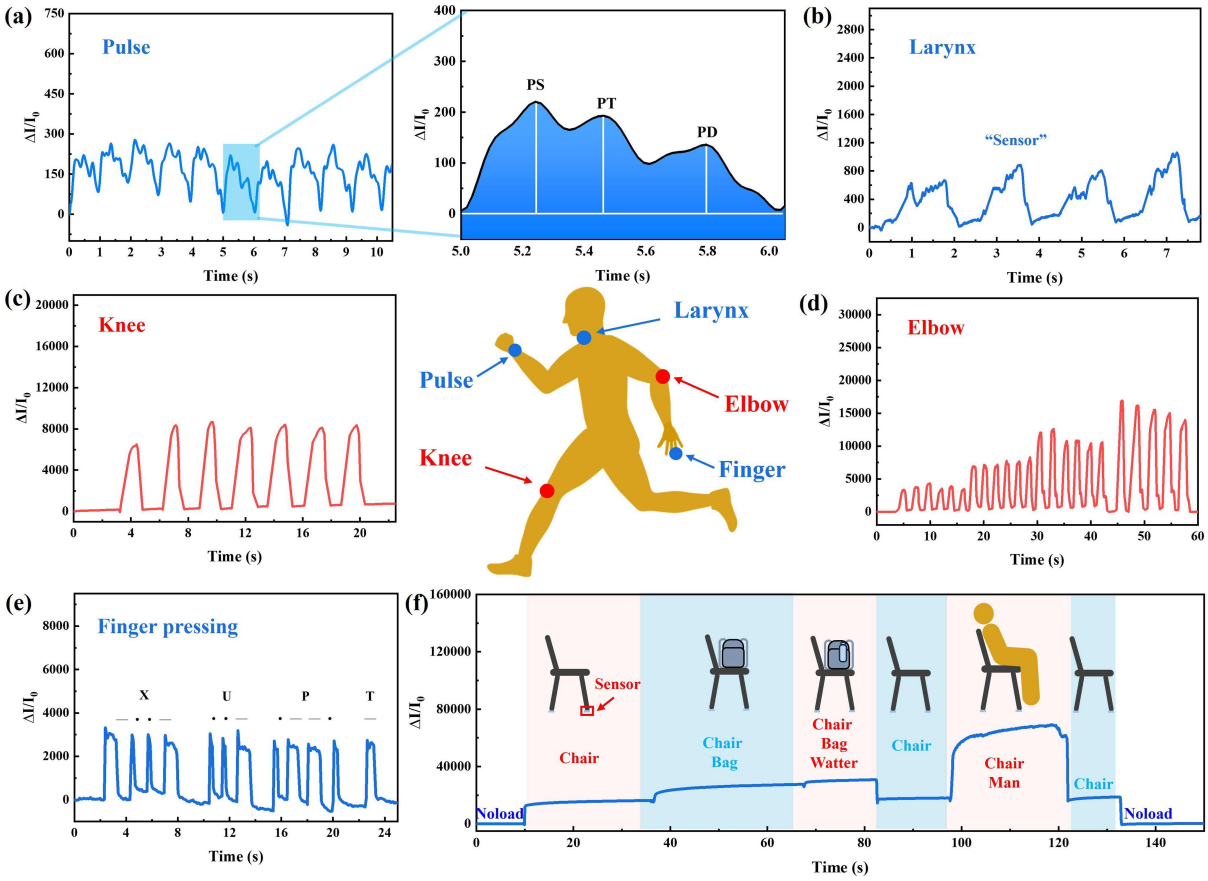

Figure 5 (Color online) Response of pressure sensors detecting (a) pulse, (b) larynx vibration, (c) knee bending, (d) elbow bending, and (e) finger presses. (f) The sensor was placed under the chair leg to detect the response to changes in pressure.

3.4 Application of the flexible pressure sensor

The flexible pressure sensor exhibited considerable application potential in monitoring the full range of human physiological signals from low to high pressure because of its excellent flexibility, high sensitivity, ultrawide linear sensing range, fast response, and excellent stability. In validating this potential, the sensor was attached to different parts of the human body to monitor a wide range of physiological signals and physical movements. First, the pressure sensor responds well to weak physiological signals such as pulses and sounds. The pulse is an essential physiological signal in the human body. By analyzing the pulse frequency, intensity, and reflection, various medical information, such as aging or hardening of blood vessels, can be obtained to diagnose and prevent cardiovascular diseases. The pressure sensor was applied to the radial artery for pulse detection (Figure 5(a)). The pulse rate of the volunteer was 66 beats/min. In addition, the characteristics of shock wave (P), tidal wave (T), and two-way scattering wave (D) could be clearly recognized in the amplified single pulse cycle (Figure 5(a)), indicating the high sensitivity of the sensor. The pressure sensor can also be connected to the larynx to monitor phonation. As shown in Figure 5(b), the sensor can detect the pressure change in the larynx when the volunteer utters "sensor". When the word was repeated several times, the uniformity of the response waveform was observed, indicating that the sensor has good stability and reliability. Therefore, the pressure sensor can be applied in speech recognition.

Apart from small physiological signals, the pressure sensor also responds excellently to large movements of the human body (e.g., knee and elbow bending and finger pressing). As shown in Figure 5(c), the relative current change increases when the knee is bent and returns to the initial value when the knee is straightened. As shown in Figure 5(d), different degrees of elbow flexion can be successfully distinguished by the difference in the peak value of the current wave, confirming its considerable application potential in human motion monitoring. As shown in Figure 5(e), Morse code is sent by pressing the sensor with a finger. The time-dependent curve of the relative current change forms different combinations of "–" and "·" corresponding to the letters "XUPT" in Morse code. The different combinations of "–" and "·" in Morse code are indicated by longer or shorter presses, respectively.

Finally, pressure sensors were mounted under the legs of the chair to detect the pressure of different objects

placed on the chair and to evaluate their ability to detect a wider range of pressures (Figure 5(f)). When a 500-g bottle of water was added to the chair with a bag, the sensor could detect the change in pressure. The sensor could also detect a change in pressure when a person (60 kg) sat on the chair. Eventually, the sensor detected pressure signals from the sole during walking (Figure S19). The pressure underfoot during walking was approximately 300 kPa.

4 Conclusion

In this study, a BCISPC for flexible pressure sensors was proposed. The effects of the preparation process and PCL particle size on the percolation threshold of BCISPC were investigated. The conductive self-healing efficiency of the composite under different healing conditions was tested, and its self-healing principles were analyzed. BCISPC had an electrical conductivity of 13.3 S/m, a high electrical self-healing efficiency of 94.2%, and a high HR of 314%/min. A self-healing flexible pressure sensor was prepared using the microstructured BCISPC. The optimization of the microstructured BCISPC endowed the sensor with a high sensitivity of 159.4 kPa^{-1} and a wide linear measurement range of 0–500 kPa. Meanwhile, the sensor had a fast response time (34 ms) and good cycling durability (1000 cycles). In addition, the sensor could detect a full range of pressure signals, from low to high. Given the high performance of the sensor, it has various applications in wearable electronics, medical monitoring, and human-machine interfaces.

Acknowledgements This work was supported by National Natural Science Foundation of China (Grant No. 92271201), Natural Science Basic Research Program of Shaanxi (Grant No. 2024JC-JCQN-61), Natural Science Basic Research Program of Shaanxi (Grant No. 2025JC-YBQN-941), and Scientific Research Program Funded by Shaanxi Provincial Education Department (Grant No. 24JK0656).

Supporting information Appendix A. The supporting information is available online at info.scichina.com and link.springer.com. The supporting materials are published as submitted, without typesetting or editing. The responsibility for scientific accuracy and content remains entirely with the authors.

References

1 He S X, Wu J, Duan Y H, et al. Soft-template synthesis of hierarchically porous structured polydimethylsiloxane toward flexible capacitive pressure sensor. Sci China Tech Sci, 2023, 66: 2696–2706
2 Zheng X, Zhang S, Zhou M, et al. MXene functionalized, highly breathable and sensitive pressure sensors with multi-layered porous structure. Adv Funct Mater, 2023, 33: 2214880
3 Wang P, Liang J, Tian W, et al. Transient piezoresistive sensors based on tolerable, safe, and semiconductive polypyrrole/vermiculite/alginate frameworks. Sci China Mater, 2024, 67: 580–587
4 Lu X, Meng X, Shi Y, et al. Multilayer microstructured high-sensitive ultrawide-range flexible pressure sensor with modulus gradient. IEEE Trans Electron Devices, 2022, 69: 2030–2037
5 Roy S, Deo K A, Lee H P, et al. 3D printed electronic skin for strain, pressure and temperature sensing. Adv Funct Mater, 2024, 34: 2313575
6 Zheng W D, Liu H P, Liu X F, et al. Data-driven electrical resistance tomography for robotic large-area tactile sensing. Sci China Inf Sci, 2024, 67: 199201
7 Li Y, Zhang W, Zhao C, et al. Breaking the saturation of sensitivity for ultrawide range flexible pressure sensors by soft-strain effect. Adv Mater, 2024, 36: 2405405
8 Gao J, Hu M, Sun H, et al. Disposable and flexible smart electronic tapes for long-term biopotential monitoring. npj Flex Electron, 2025, 9: 6
9 Li Y, Wei Y, Yang Y, et al. The soft-strain effect enabled high-performance flexible pressure sensor and its application in monitoring pulse waves. Research, 2022, 2022: 2
10 He J R, Qu Y S, Chen S Y, et al. Highly sensitive flexible strain sensor based on the two-dimensional semiconductor tellurium with a negative gauge factor. Sci China Inf Sci, 2024, 67: 172401
11 Meng X, Lu X, Shi Y, et al. Pressure-controlled thermochromic electronic skin with adjustable memory time during fabrication for in situ pressure display application. IEEE Trans Instrum Meas, 2022, 71: 1–9
12 Xia Y, Huang P, Lin X, et al. The piezoresistive pressure sensors based on ITO nanocrystalline-plant fiber composite. Sci China Mater, 2023, 66: 3922–3930
13 Lin J, Ai Y, Li W, et al. Flexible multi-modal sensors based on CNT hollow spheres/PDMS composites for human motion recognition and colloid concentration detection. Compos Sci Tech, 2023, 237: 110005
14 Yang Y F, Yang H, Shang J C, et al. A high-sensitivity flexible PDMS@rGO-based pressure sensor with ultra-wide working range based on bioinspired gradient hierarchical structure with coplanar electrodes. Compos Sci Tech, 2023, 240: 110078
15 Xu D, Zhou P, Yu H, et al. Bioinspired fabrication of graphene/PDMS composite materials for high-performance flexible pressure sensor. Sci China Mater, 2025, 68: 1184–1195
16 Jia X Y, Mu J L, Wu Q, et al. Research on thermal cyclization polyacrylonitrile enhanced piezoelectric performances of a flexible electronic skin sensor. Sci China Tech Sci, 2024, 67: 3855–3866
17 Yao B, He S, Wang R, et al. Cephalopod-inspired soft composite with liquid metal inclusions for tunable infrared modulation. J Materiomics, 2025, 11: 101012
18 Yao B, Lü X, Wang Y, et al. Ultrasensitive, highly stable, and stretchable strain sensor using gated liquid metal channel. Adv Funct Mater, 2024, 34: 2314298
19 Sun L, Huang H, Zhang L, et al. Spider-silk-inspired tough, self-healing, and melt-spinnable ionogels. Adv Sci, 2024, 11: 2305697
20 Zhao Y, Ohm Y, Liao J, et al. A self-healing electrically conductive organogel composite. Nat Electron, 2023, 6: 206–215
21 Li Y, Liu L, Zhao C, et al. Multifunctional double network hydrogel with multi-directional actuation and high-precision sensing. Sens Actuat B-Chem, 2025, 422: 136669
22 Wu S, Wang B, Chen D, et al. Highly sensitive and self-healing conductive hydrogels fabricated from cationic cellulose nanofiber-dispersed liquid metal for strain sensors. Sci China Mater, 2023, 66: 1923–1933
23 Zhang Z P, Rong M Z, Zhang M Q. Self-healable functional polymers and polymer-based composites. Prog Polym Sci, 2023, 144: 101724
24 Guo W Y, Ma M G. Conductive nanocomposite hydrogels for flexible wearable sensors. J Mater Chem A, 2024, 12: 9371–9399

25 Liu Y, Wang F, Hu Z, et al. Applications of cellulose-based flexible self-healing sensors for human health monitoring. Nano Energy, 2024, 127: 109790
26 Li R, Fan T, Chen G, et al. Highly transparent, self-healing conductive elastomers enabled by synergistic hydrogen bonding interactions. Chem Eng J, 2020, 393: 124685
27 Min J, Zhou Z, Wang H, et al. Room temperature self-healing and recyclable conductive composites for flexible electronic devices based on imine reversible covalent bond. J Alloys Compd, 2022, 894: 162433
28 Yu T, Lü X, Bao W. High electrical self-healing flexible strain sensor based on MWCNT- polydimethylsiloxane elastomer with high gauge factor and wide measurement range. Compos Sci Tech, 2023, 238: 110049
29 Kong L, Yang Y, Lin Z, et al. A ENR-based conductive film integrating electricity-triggered self-healing, damage detection and high sensitivity for flexible sensors. Chem Eng J, 2024, 479: 147624
30 Liu R, Bi S, Zhang L, et al. Flexible and antibacterial conductive hydrogels based on silk fibroin/polyaniline/AgNPs for motion sensing and wound healing promotion under electrical stimulation. J Mater Chem B, 2024, 12: 10346–10356
31 Zheng Y, Li Y, Li Z, et al. The effect of filler dimensionality on the electromechanical performance of polydimethylsiloxane based conductive nanocomposites for flexible strain sensors. Compos Sci Tech, 2017, 139: 64–73
32 Fang M, Li D, Lin H, et al. Flexible and recyclable conductive composite based on few-layered graphene with excellent self-healing capability. Eur Polym J, 2018, 108: 536–541
33 Lu Y, Liu Z, Yan H, et al. Ultrastretchable conductive polymer complex as a strain sensor with a repeatable autonomous self-healing ability. ACS Appl Mater Interfaces, 2019, 11: 20453–20464
34 Pu W, Fu D, Wang Z, et al. Realizing crack diagnosing and self-healing by electricity with a dynamic crosslinked flexible polyurethane composite. Adv Sci, 2018, 5: 1800101
35 Song Y, Li J, Song G, et al. Superior strength, highly stretchable, bionic self-healing polyurethane and its composites for flexible conductivity and self-cleaning applications. Compos Part B-Eng, 2024, 280: 111457
36 Tang M, Zheng P, Wang K, et al. Autonomous self-healing, self-adhesive, highly conductive composites based on a silver-filled polyborosiloxane/polydimethylsiloxane double-network elastomer. J Mater Chem A, 2019, 7: 27278–27288
37 Vu V P, Kim S H, Mai V D, et al. Bio-based conductive polyurethane composites derived from renewable castor oil with enhanced self-healing ability for flexible supercapacitors. J Mater Sci Tech, 2024, 188: 44–61
38 Wang T, Zhang Y, Liu Q, et al. A self-healable, highly stretchable, and solution processable conductive polymer composite for ultrasensitive strain and pressure sensing. Adv Funct Mater, 2018, 28: 1705551
39 Wang Y, Wang Y, Li T T, et al. Preparation and properties of polyaniline self-healing conductive materials based on hydrogen bonding and electrostatic interaction forces. ACS Appl Polym Mater, 2023, 5: 9585–9593
40 Wei J, Peng H, Zhu Y, et al. Mechanical and electrical dual-repairing agents for flexible conductors based on biphasic liquid metal-polymer composites. ACS Appl Polym Mater, 2023, 6: 69–78
41 Yang P K, Zhu X L, Huang L, et al. Skin-inspired electret nanogenerator with self-healing abilities. Cell Rep Phys Sci, 2020, 1: 100185
42 Zhang Q, Liu L, Pan C, et al. Thermally sensitive, adhesive, injectable, multiwalled carbon nanotube covalently reinforced polymer conductors with self-healing capabilities. J Mater Chem C, 2018, 6: 1746–1752
43 Zhang Z, Tang L, Chen C, et al. Liquid metal-created macroporous composite hydrogels with self-healing ability and multiple sensations as artificial flexible sensors. J Mater Chem A, 2021, 9: 875–883
44 Gong Z, Wang X, Chen X, et al. Biobased foamed thermoplastic vulcanizate with good electromagnetic interference and self-healing performance. ACS Sustain Chem Eng, 2023, 11: 9243–9254
45 Dai W, Wang J, Xiang K, et al. Highly stretchable, ultra-sensitive, and self-healable multifunctional flexible conductive hydrogel sensor for motion detection and information transmission. ACS Appl Mater Interfaces, 2023, 15: 29499–29510
46 Yin H, Chen L, Liu F, et al. MXene-based conductive hydrogels with toughness and self-healing enhancement by metal coordination for flexible electronic devices. Mater Today Phys, 2024, 47: 101537
47 Wang Y, Park B S, Vu V P, et al. Self-healing conducting composite electrodes derived from chemical recycling of PET plastic wastes for flexible supercapacitors. Polym Eng Sci, 2025, 65: 1854–1867
48 Chang C W, Wu C T, Lo T Y, et al. Alkaline-responsive, self-healable, and conductive copolymer composites with enhanced mechanical properties tailored for wearable tech. Small, 2024, 20: 2402472
49 Myshkin N K, Braunovich M, Konchits V V. The mechanics and tribophysics of electrical contacts. J Frict Wear, 2015, 36: 454–467